12-23-2013

Spatial spectrograms of vibrating atomic force microscopy cantilevers coupled to sample surfaces

Ryan Wagner
Purdue University, Birck Nanotechnology Center, rbwagner@purdue.edu

Arvind Raman
Purdue University, Birck Nanotechnology Center, raman@purdue.edu

Roger Proksch
Asylum Res

Wagner, Ryan; Raman, Arvind; and Proksch, Roger, "Spatial spectrograms of vibrating atomic force microscopy cantilevers coupled to sample surfaces" (2013). *Birck and NCN Publications.* Paper 1538.
http://dx.doi.org/10.1063/1.4840116

Spatial spectrograms of vibrating atomic force microscopy cantilevers coupled to sample surfaces

Ryan Wagner, Arvind Raman, and Roger Proksch

Citation: Applied Physics Letters **103**, 263102 (2013); doi: 10.1063/1.4840116
View online: http://dx.doi.org/10.1063/1.4840116
View Table of Contents: http://scitation.aip.org/content/aip/journal/apl/103/26?ver=pdfcov
Published by the AIP Publishing

Spatial spectrograms of vibrating atomic force microscopy cantilevers coupled to sample surfaces

Ryan Wagner,[1] Arvind Raman,[1,a)] and Roger Proksch[2,b)]
[1]*Birck Nanotechnology Center, 1205 W. State Street, Purdue University, West Lafayette, Indiana 47907, USA*
[2]*Asylum Research, 6310 Hollister Ave., Santa Barbara, California 93117, USA*

(Received 23 September 2013; accepted 19 November 2013; published online 23 December 2013)

Many advanced dynamic Atomic Force Microscopy (AFM) techniques such as contact resonance, force modulation, piezoresponse force microscopy, electrochemical strain microscopy, and AFM infrared spectroscopy exploit the dynamic response of a cantilever in contact with a sample to extract local material properties. Achieving quantitative results in these techniques usually requires the assumption of a certain shape of cantilever vibration. We present a technique that allows *in-situ* measurements of the vibrational shape of AFM cantilevers coupled to surfaces. This technique opens up unique approaches to nanoscale material property mapping, which are not possible with single point measurements alone. © *2013 AIP Publishing LLC*.
[http://dx.doi.org/10.1063/1.4840116]

Many dynamic atomic force microscopy (AFM)[1] techniques involve a vibrating microcantilever in permanent contact with a sample surface. Contact resonance (CR-AFM),[2–6] force modulation (FMM),[7,8] piezoresponse force (PFM),[9–11] electrochemical strain (ESM),[12,13] and AFM infrared spectroscopy (AFM-IR)[14] are a few pertinent examples. These techniques allow scientists to measure and map a variety of properties including elastic, viscoelastic, piezoelectric, electrochemical, and chemical properties of surfaces with nanometer scale resolution.

In typical AFM operation, the cantilever bending angle at a single laser spot position is measured.[15,16] The overall cantilever vibration shape remains unobserved. This limits many calibration and data processing techniques in AFM. For example, calculating the optical sensitivity in all AFM modes and calculating material properties in CR-AFM assume a deflection or vibration shape for the cantilever. When operating far from the sample surface the vibration shapes are often well described by theoretical beam models with boundary conditions of zero shear force and bending moment at the cantilever tip. However, when operating in contact, the boundary conditions at the tip depend sensitively on local material properties as well as the operating frequency, cantilever amplitude, tip-sample force, and contact geometry. This injects great uncertainty into the theoretical prediction of vibrating shapes. To resolve this, reliable experimental techniques are needed to determine the vibration shape of AFM cantilevers interacting with sample surfaces.

Vibrational shapes of AFM cantilevers have been studied with interferometry,[17,18] optical beams,[19–21] and scanning electron microscopy.[22] This prior work has described vibrating shapes out of contact with a sample or during an intermittent contact situation. More importantly, most of this prior work has required the use of an additional measurement system such as an interferometer to measure cantilever vibration. Here, we develop an optical beam method for measuring the *in-situ* vibrational shape of an AFM cantilever on a standard commercial AFM without interfacing an additional measurement system and used this method to study CR-AFM techniques. This technique provides an important tool for the visualization the vibration of AFM cantilevers.

Our method allows us to quickly and efficiently validate the dynamics of models used to extract material properties from AFM data. We compare the experimental and theoretical responses and observe a few interesting differences between the predicted and actual response. These comparisons are used to validate existing CR-AFM modeling techniques and provide insight into additional physics that could be added to such models. Validation and improvement of these models will lead to more accurate predictions of material properties with CR-AFM.

A Cypher AFM (Asylum Research, Santa Barbara, CA) with a standard 30 μm laser spot was used for AFM measurements. Experiments were performed in a glove box with controlled temperature and relative humidity. A Hitachi High-Technologies Corporation (Tokyo, Japan) s-4800 field emission scanning electron microscope (SEM) was used to capture SEM images of the cantilevers. AppNano (Santa Clara, CA) FORT cantilevers, which have a first free resonance frequency at about 70 kHz and a stiffness of about 2 N/m, and Nanosensors (Neuchatel, Switzerland) NCLR cantilevers, which have a first free resonance frequency of about 180 kHz and a stiffness of about 40 N/m are the two cantilever types used in the experiments. The actual cantilever stiffness was determined using the corrected thermal method.[23–25] The photodiode sensitivity was determined from a force-displacement curve on a stiff sample. The cantilever stiffness and photodiode sensitivity was used to compute the force applied to the sample. For the NCLR cantilevers, a force of 1000 nN was applied to the sample and for the FORT cantilevers a force of 100 nN was applied to the sample. These forces correspond to about 30 nm of cantilever deflection.

Several additional parameters are needed for the comparison of experiment and theory. The evaluation of these

a)Electronic mail: raman@purdue.edu.
b)Electronic mail: Roger.Proksch@oxinst.com.

parameters is described as follows. The cantilever dimensions, tip dimensions, and tip location was determined based on SEM images. The tip mass (m_t) was determined by computing the tip volume and multiplying by the density of silicon (2.3 g/cm^3). The cantilever mass (m_c) was determined from the first free resonance frequency, cantilever stiffness, and tip mass. The cantilever tilt angle (θ_c) relative to the sample of 11° was determined from the AFM manufacturer's specifications. After the experiments were finished the tip radius of the AFM cantilever tip was measured with SEM to be 220 nm for the NCLR cantilever and 90 nm for the FORT cantilever. Silicon, with a modulus of 160 GPa and SU-8 polymer, with a nominal storage modulus of 5 GPa and a nominal loss modulus of 50 MPa were used as samples. It should be noted that the properties of SU-8 thin films vary with both frequency[26] and film thickness.[27]

The basic measurement technique is described as follows. First, the cantilever was brought into contact with the sample at a constant normal load. Next, the cantilever was held at the constant load for a few minutes to allow the AFM system to come into mechanical and electrical equilibrium. The feedback between the cantilever and the sample surface was then turned off. The location of AFM laser spot position on the cantilever was then scanned along the length of the cantilever. The laser position was adjusted by standard commercial laser positioning system that comes with the Cypher AFM system. The positioning system works by using electric motors to move the laser source, mirrors, and mounting of the optical beam system. The system is controlled by the Asylum Research AFM controller and software. The center of the laser spot can be accurately and repeatability positioned within about 1 μm. At each laser spot position the excitation frequency applied to a transducer below the sample was swept and the photodiode amplitude and phase recorded. The photodiode amplitude and phase was then plotted as a function of spot position and frequency. This results in a "spectrogram" describing the shape of dynamic response of the cantilever. The time it takes to capture a spectrogram depends strongly on how many points on the cantilever are measured and how fast the cantilever excitation frequency is swept. For the data in this paper, it took about 10 min to capture a single spectrogram. Because the feedback between the cantilever and sample was turned off there is some drift in the force applied to the cantilever. This drift was monitored with a closed loop stage attached to the Z-piezo. A schematic of the experimental setup is shown in Figure 1(a). In contrast to earlier mode measurement approaches, these measurements are fully integrated into a standard commercial AFM system. The optical lever slope sensitivity of the spectrogram measurement exactly matches that of the AFM system since it is made using the same detector.

To interpret the experimental results it is necessary to understand the output of the AFM detection system. Most AFMs use an optical beam deflection (OBD) system to detect the cantilever response. In OBD, the voltage output of the photodiode is approximately proportional to the slope of the cantilever at the position of measurement.[28,29] For the dynamic AFM modes mentioned above a lock-in amplifier is used to measure amplitude and phase of the photodiode signal at the drive frequency; therefore, the resulting spectrograms are a measurement of the amplitude of slope (slope amplitude, A_s) of the AFM cantilever as a function of laser spot position on the cantilever and the excitation frequency of the sample. In contrast, a similar experiment with an interferometer based system would measure the amplitude of the cantilever displacement (displacement amplitude, A_d).[17,18] A sketch of the slope amplitude for the first two resonance modes for a cantilever far from a sample surface are shown in Figure 1(b).

To relate the experimental observed parameters, such as resonance frequency, amplitude, and phase to material properties, such as elastic and viscoelastic modulus a model of the cantilever response is needed. In CR-AFM, the predicted material properties depend on which model is used to interpret the data. Different models, with a variety of beam types, boundary conditions, and fluid damping, can be used to predict material properties. We compared the measured spectrograms to theoretical spectrograms predicted by the uniform damped Euler-Bernoulli beam model with mass, spring, and damper boundary conditions.[30] Tip mass (m_t), tip inertia (I_t), normal contact stiffness (k_n), lateral contact stiffness (k_l), normal damping (c_n), lateral damping (c_l), and cantilever excitation (u) are included as boundary conditions. The free vibration solution to these equations gives a characteristic equation, which provides a relationship between resonance frequencies and boundary conditions. The forced vibration solution to these equations can reproduce spectrograms for comparison to experiments. The model for a surface coupled AFM cantilever is shown in Figure 1(c). The normal contact stiffness and normal damping was computed from the AFM tip radius, the applied normal force, the sample storage and

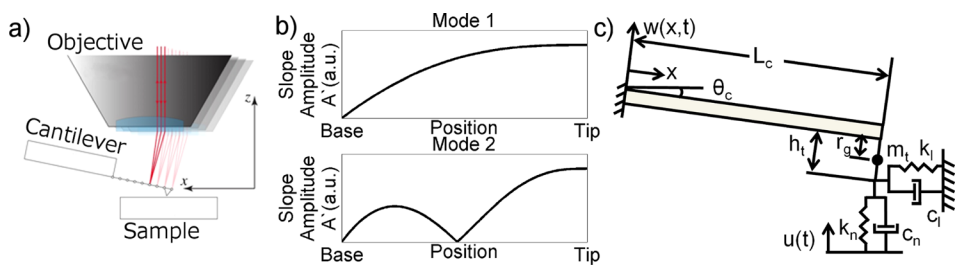

FIG. 1. (a) Experimental schematic. The laser position is scanned along the length of the cantilever and the excitation frequency is swept. (b) Slope amplitude for the first two modes for a cantilever far from the sample surface. (c) Schematic showing boundary conditions used in Euler-Bernoulli beam model of cantilever. L_c is the cantilever length, θ_c is the tilt angle of the cantilever, w is the displacement of the cantilever, x is the position along the length of the cantilever, h_t is the height of the tip, k_n is the contact stiffness normal to the sample surface, k_l is the contact stiffness lateral to the sample surface, c_n is the contact damping normal to the sample surface, c_l is the contact damping lateral to the sample surface, m_t is the mass of the tip, and r_g is the radius of gyration of the tip.

loss modulus, and the DMT contact mechanics model.[31,32] The lateral contact stiffness and lateral damping was assumed to be 80% of the normal stiffness and damping. This is true for an isotropic material with a Poisson's ratio of 0.3.

Experimental and theoretical spectrograms for two cantilevers and two samples are shown in Figure 2. The experimental parameters used to predict the theoretical spectrograms are given in Table I. The spectrograms plot spot position on the y-axis, frequency on the x-axis, and cantilever slope amplitude divided by sample excitation amplitude or slope phase relative to the drive signal on the color axis. In the slope amplitude spectrograms, the bright vertical lines correspond to resonance frequencies and dark curves correspond to the antinode frequencies and locations. In the slope phase spectrograms, phase jumps are seen as resonance frequencies and antinode locations change according to laser spot position and excitation frequency. In Figures 2(a) and 2(i), there is a resonance at a frequency of 700 kHz. This resonance has a minimum in slope amplitude about halfway along its length at its slope amplitude antinode. This minimum in slope amplitude corresponds to a local maximum in displacement amplitude. The antinode in slope amplitude starts at a frequency of 400 kHz at the location of the tip and moves towards the base of the cantilever with increasing frequency.

Several interesting conclusions can be made by comparing the experimental and theoretical spectrograms. Most aspects of the theoretical and experimental spectrograms are in agreement. For example, the shape of the slope amplitude

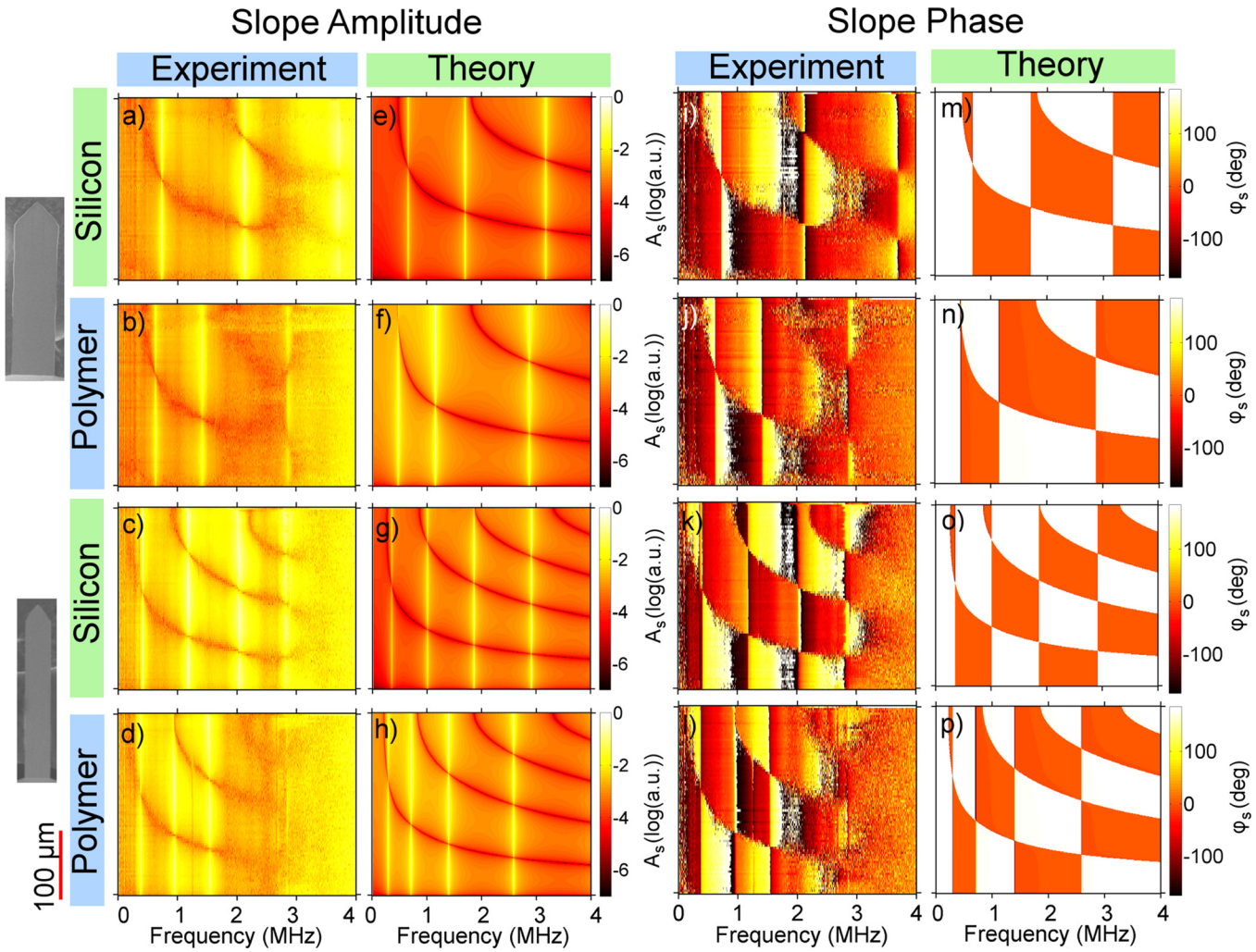

FIG. 2. Experimentally measured and theoretically predicted slope amplitude (log color scale) and slope phase spectrograms. (a) Experimental slope amplitude for a stiff lever (NCLR, 40 N/m) on a stiff sample (Silicon, Force ~1000 nN). (b) Experimental slope amplitude for a stiff lever (NCLR, 40 N/m) on a soft sample (SU-8, Force ~1000 nN). (c) Experimental slope amplitude for a soft lever (FORT, 3.2 N/m) on a stiff sample (Silicon, Force ~100 nN). (d) Experimental slope amplitude for a soft lever (FORT, 3.2 N/m) on a soft sample (SU-8, Force ~100 nN). (e) Theoretical slope amplitude for a stiff lever (NCLR, 40 N/m) on a stiff sample (Silicon, Force ~1000 nN). (f) Theoretical slope amplitude for a stiff lever (NCLR, 40 N/m) on a soft sample (SU-8, Force ~1000 nN). (g) Theoretical slope amplitude for a soft lever (FORT, 3.2 N/m) on a stiff sample (Silicon, Force ~100 nN). (h) Theoretical slope amplitude for a soft lever (FORT, 3.2 N/m) on a soft sample (SU-8, Force ~100 nN). (i) Experimental slope phase for a stiff lever (NCLR, 40 N/m) on a stiff sample (Silicon, Force ~1000 nN). (j) Experimental slope phase for a stiff lever (NCLR, 40 N/m) on a soft sample (SU-8, Force ~1000 nN). (k) Experimental slope phase for a soft lever (FORT, 3.2 N/m) on a stiff sample (Silicon, Force ~100 nN). (l) Experimental slope phase for a soft lever (FORT, 3.2 N/m) on a soft sample (SU-8, Force ~100 nN). (m) Theoretical slope phase for a stiff lever (NCLR, 40 N/m) on a stiff sample (Silicon, Force ~1000 nN). (n) Theoretical slope phase for a stiff lever (NCLR, 40 N/m) on a soft sample (SU-8, Force ~1000 nN). (o) Theoretical slope phase for a soft lever (FORT, 3.2 N/m) on a stiff sample (Silicon, Force ~100 nN). (p) Theoretical slope phase for a soft lever (FORT, 3.2 N/m) on a soft sample (SU-8, Force ~100 nN). The y-axis scale bar applies for all subfigures.

TABLE I. Table of parameter used to calculate theoretical spectrograms. Parameters based on calibration experiments and assumed material properties of silicon and SU-8. $\omega_{f,1}$ is the first cantilever resonance frequency far from the sample and $Q_{1,f}$ is the quality factor of the first cantilever resonance frequency far from the sample. Other parameters are as given in Figure 1(c).

Figure number	L (μm)	k_c $\left(\frac{\text{nN}}{\text{nm}}\right)$	m_c (pg)	$\omega_{1,f}$ (kHz)	$Q_{1,f}$	m_t (pg)	I_t (pg μm^2)	h_t (μm)	k_n $\left(\frac{\text{nN}}{\text{nm}}\right)$	k_l $\left(\frac{\text{nN}}{\text{nm}}\right)$	$c_n\omega$ $\left(\frac{\text{nN}}{\text{nm}}\right)$	$c_l\omega$ $\left(\frac{\text{nN}}{\text{nm}}\right)$	θ_c (deg)	u (nm)
A	225	40	158	158.1	290	0.9	0.18	13	2250	1800	0	0	11	1
B	225	40	158	158.1	290	0.9	0.18	13	368	294	3.4	2.7	11	1
C	225	3.2	60	72.3	130	0.45	0.11	15	775	620	0	0	11	1
D	225	3.2	60	72.3	130	0.45	0.11	15	127	102	1.2	0.9	11	1

at the resonance frequencies, and the location of antinodes as a function of excitation frequency all agree well between experiment and theory. However, some differences between experiment and theory can be observed. These differences allow for analysis of model form uncertainty, which can be an important source of uncertainty in CR-AFM measurements. Including more complex damping models, a more accurate model of the physical shape of the cantilever, or the effects of finite laser spot size are potential model improvements that could reduce model form uncertainty.

The first potential source of model form uncertainty is the applied damping models. We have used a linear viscous air damping model to model the fluid damping experienced by the cantilever and a linear dashpot to model the damping associated with the tip-sample interaction. This damping model is not sufficient to capture all aspects of the cantilever response. This can be seen by observing the maximum bending energy of the cantilever beam ($BE_{max} = \int_0^L (\frac{\delta A_s}{\delta x})^2 dx$[33]) as a function of excitation frequency as shown in Figure 3(a). In the experimental data, the potential energy of the cantilever near the resonance frequencies decreases with increasing frequency. In the theoretical data, the potential energy of the cantilever near resonance is almost constant with increasing frequency. This difference might be corrected by including effects such as squeeze film damping,[34] or frequency dependent fluid,[35] or sample damping.

A second potential source of model form uncertainty is variations of the actual cantilever from that of ideal Euler-Bernoulli beam. The physical shape of the cantilever is different from a uniform Euler-Bernoulli beam in three ways: a picket at the end of the cantilever, trapezoidal cantilever cross sections, and variation in thickness along the length of the cantilever from manufacturing imperfections. These uncertainties could be addressed by applying a more complex form of the Euler-Bernoulli beam equation or through finite element modeling.[36]

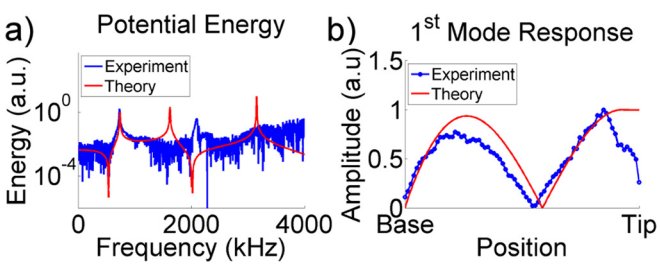

FIG. 3. (a) Comparison of experiment and theory for bending energy of the cantilever as a function of frequency for the 40 N/m lever on Silicon. Experimental potential energy decreases faster than theoretical potential energy. This implies that the damping model used is inadequate to capture the actual system response. (b) Comparison of experiment and theory for the slope amplitude of first resonance mode for the 40 N/m lever on silicon. The disagreement near the end of the cantilever is due to changes in the photodiode sum signal as the laser moves off the end of the cantilever.

A third potential source of model from uncertainty is the effect of finite laser spot size on the experimental measurements. It is known that the measured cantilever response is affected by the finite size of the laser.[29,37] This shows up in the spectrogram data in two ways. First, the slope as a function of spot position is not exactly the slope at that position, but rather an average slope computed over the size of the laser spot. Second, near the end of the cantilever the laser spot starts to fall off the edge of the cantilever. This reduces the photodiode sum signal causes the sensitivity of the optical beam system to decrease. This effect can be clearly seen in Figure 3(b), in which theory and experiment agree well far from the end of the cantilever but diverge near the tip.

Using *in-situ* experiments on a standard commercial AFM system, we have experimentally measured the shape of the cantilever vibration in CR-AFM. In principle, this provides a pathway for validation of existing CR-AFM models and deeper insight into the forces acting on the AFM cantilever. We analyzed cantilever vibrational shapes for two cantilevers and two samples. Agreement between experimental cantilever shapes and those predicted with the standard CR-AFM model is reasonably good, providing validation for use of the discussed model. However, some details, such as under-predicted resonance frequencies, point load effects, and damping effects, were shown to be different between experiment and theory. These effects might represent additional physics that could be added to existing contact resonance models. It is hoped that this work will provide motivation for the further development of surface coupled cantilever modeling and a pathway towards the validation of existing contact resonance modeling techniques.

The authors acknowledge the financial support of the USFS Forest products laboratory, the assistance of the staff of Asylum Research (Santa Barbara, CA) and the Birck Nanotechnology Center (West Lafayette, IN), and discussions with Professor Robert Moon, Purdue University.

[1]G. Binnig and C. Quate, Phys. Rev. Lett. **56**, 930–933 (1986).
[2]U. Rabe and W. Arnold, Appl. Phys. Lett. **64**, 1493–1495 (1994).
[3]U. Rabe, K. Janser, and W. Arnold, Rev. Sci. Instrum. **67**, 3281–3293 (1996).

[4]K. Yamanaka, H. Ogiso, and O. Kolosov, Appl. Phys. Lett. **64**, 178–180 (1994).
[5]K. Yamanaka, Y. Maruyama, T. Tsuji, and K. Nakamoto, Appl. Phys. Lett. **78**, 1939–1941 (2001).
[6]A. Gannepalli, D. G. Yablon, A. H. Tsou, and R. Proksch, Nanotechnology **22**, 355705 (2011).
[7]P. Maivald, H. J. Butt, S. A. C. Gould, C. B. Prater, B. Drake, J. A. Gurley, V. B. Elings, and P. K. Hansma, Nanotechnology **2**, 103–106 (1991).
[8]X. Xu, M. Koslowski, and A. Raman, J. Appl. Phys. **111**, 054303 (2012).
[9]P. Güthner and K. Dransfeld, Appl. Phys. Lett. **61**, 1137–1139 (1992).
[10]T. Hidaka, T. Maruyama, M. Saitoh, N. Mikoshiba, M. Shimizu, T. Shiosaki, L. A. Wills, R. Hiskes, S. A. Dicarolis, and J. Amano, Appl. Phys. Lett. **68**, 2358–2359 (1996).
[11]S. Xie, A. Gannepalli, Q. N. Chen, Y. Liu, Y. Zhou, R. Proksch, and J. Li, Nanoscale **4**, 408–413 (2012).
[12]L. Y. Beaulieu, T. D. Hatchard, A. Bonakdarpour, M. D. Fleischauer, and J. R. Dahn, J. Electrochem. Soc. **150**, A1457–A1464 (2003).
[13]N. Balke, S. Jesse, A. N. Morozovska, E. Eliseev, D. W. Chung, Y. Kim, L. Adamczyk, R. E. Garcia, N. Dudney, and S. V. Kalinin, Nat. Nanotechnol. **5**, 749–754 (2010).
[14]B. Knoll and F. Keilmann, Nature **399**, 134–137 (1999).
[15]G. Meyer and N. M. Amer, Appl. Phys. Lett. **53**, 1045–1047 (1988).
[16]S. Alexander, L. Hellemans, O. Marti, J. Schneir, V. Elings, P. K. Hansma, M. Longmire, and J. Gurley, J. Appl. Phys. **65**, 164–167 (1989).
[17]M. Hoummady, E. Farnault, T. Yahiro, and H. Kawakatsu, J. Vac. Sci. Technol. B **15**, 1539–1542 (1997).
[18]M. Spletzer, A. Raman, and R. Reifenberger, J. Micromech. Microeng. **20**, 085024 (2010).
[19]T. E. Schäffer, J. P. Cleveland, F. Ohnesorge, D. A. Walters, and P. K. Hansma, J. Appl. Phys. **80**, 3622–3627 (1996).
[20]J. Tamayo, V. Pini, P. Kosaka, N. F. Martinez, O. Ahumada, and M. Calleja, Nanotechnology **23**, 315501 (2012).
[21]X. Zhou, J. Fu, and F. Li, J. Appl. Phys. **114**, 064301 (2013).
[22]H. Sturm, M.-A. Schrter, and C. Weimann, Microelectron. Eng. **98**, 492–496 (2012).
[23]J. L. Hutter and J. Bechhoefer, Rev. Sci. Instrum. **64**, 1868–1873 (1993).
[24]H. J. Butt and M. Jaschke, Nanotechnology **6**, 1–7 (1995).
[25]R. Proksch, T. E. Schäffer, J. P. Cleveland, R. C. Callahan, and M. B. Viani, Nanotechnology **15**, 1344 (2004).
[26]J. Le Rouzic, P. Delobelle, P. Vairac, and B. Cretin, Eur. Phys. J.: Appl. Phys. **48**, 11201 (2009).
[27]J. Hossenlopp, L. Jiang, R. Cernosek, and F. Josse, J. Polym. Sci., Part B: Polym. Phys. **42**, 2373–2384 (2004).
[28]T. E. Schäffer and P. K. Hansma, J. Appl. Phys. **84**, 4661–4666 (1998).
[29]T. E. Schäffer and H. Fuchs, J. Appl. Phys. **97**, 083524 (2005).
[30]U. Rabe, *Applied Scanning Probe Methods II* (Springer, 2006), pp. 37–90.
[31]B. Derjaguin, V. Muller, and Y. Toporov, J. Colloid Interface Sci. **53**, 314–326 (1975).
[32]A. Raman, S. Trigueros, A. Cartagena, A. P. Z. Stevenson, M. Susilo, E. Nauman, and S. A. Contera, Nat. Nanotechnol. **6**, 809–814 (2011).
[33]S. Rao, *Mechanical Vibrations* (Pearson Prentice Hall, 2004).
[34]R. C. Tung, J. W. Lee, H. Sumali, and A. Raman, J. Micromech. Microeng. **21**, 025003 (2011).
[35]J. E. Sader, J. Appl. Phys. **84**, 64–76 (1998).
[36]J. P. Killgore and D. C. Hurley, Nanotechnology **23**, 055702 (2012).
[37]T. E. Schaffer, Nanotechnology **16**, 664–670 (2005).